論文 / 著書情報
Article / Book Information

Title	In-situ X-ray diffraction study of hydrogen absorption and desorption processes in Pd thin films: Hydrogen composition dependent anisotropic expansion and its quantitative description
Authors	Takashi Harumoto, Yusuke Ohnishi, Keishi Nishio, Takashi Ishiguro, Ji Shi, Yoshio Nakamura
Citation	AIP Advances, Vol. 7, No. 6, 065108
Pub. date	2017, 6
Creative Commons	Information is in the article.

In-situ X-ray diffraction study of hydrogen absorption and desorption processes in Pd thin films: Hydrogen composition dependent anisotropic expansion and its quantitative description

Takashi Harumoto, Yusuke Ohnishi, Keishi Nishio, Takashi Ishiguro, Ji Shi, and Yoshio Nakamura

Citation: AIP Advances **7**, 065108 (2017); doi: 10.1063/1.4986214
View online: http://dx.doi.org/10.1063/1.4986214
View Table of Contents: http://aip.scitation.org/toc/adv/7/6
Published by the American Institute of Physics

In-situ X-ray diffraction study of hydrogen absorption and desorption processes in Pd thin films: Hydrogen composition dependent anisotropic expansion and its quantitative description

Takashi Harumoto,[1,a] Yusuke Ohnishi,[2] Keishi Nishio,[2] Takashi Ishiguro,[2] Ji Shi,[1] and Yoshio Nakamura[1]
[1]*Department of Materials Science and Engineering, Tokyo Institute of Technology, Tokyo 152-8552, Japan*
[2]*Department of Materials Science and Technology, Tokyo University of Science, Tokyo 125-8585, Japan*

(Received 14 November 2016; accepted 1 June 2017; published online 13 June 2017)

The hydrogen absorption/desorption processes of (111)-textured and normal palladium (Pd) thin films of thickness ranging from 8 to 48 nm are investigated using X-ray diffractometry. The one-dimensional expansion of Pd lattice due to the substrate clamping is observed at the low hydrogen composition phase while both out-of-plane and in-plane expansions are detected at the high hydrogen composition phase. Accordingly, using a biaxial Poisson's ratio, an anisotropic expansion factor is proposed for describing such phenomenon quantitatively and the hydrogen composition dependence on this factor is investigated. [http://dx.doi.org/10.1063/1.4986214]

I. INTRODUCTION

In recent years, palladium (Pd) has attracted a growing amount of research due to its hydrogen-related catalytic and hydrogen storage properties. It is well-known that there are two phases, namely α- and β-phases, in the Pd-H system at room temperature.[1] The α-phase is the low hydrogen composition phase (up to ~2 at.% H in the case of bulk) while the β-phase is the high hydrogen composition phase (more than ~37.6 at.% H). In both α- and β-phases, their lattices are based on face-centered cubic (fcc) Pd and hydrogen atoms are incorporated randomly into the interstitial octahedral sites of fcc Pd.

Many studies have already been conducted on this α-to-β phase transformation using bulk Pd (nano-)particles, for instance, in the narrowing of the miscibility gap in Pd nanoparticles.[2] Baldi *et al.*[3] have in-situ observed on the hydrogen absorption and desorption processes in Pd nanoparticles using electron energy-loss spectroscopy. The avalanching strain and the effect of the surface structure have been revealed using diffractometry.[4–6] Reviews concerning the size effect can be found in Refs. 7 and 8.

In the case of Pd films, the α-to-β phase transformation is much more complex. In general, thin Pd films (thickness less than a few tens of nm) are resistant against hydride formation.[9,10] Also, thin epitaxial Pd films tend to exhibit reversible and coherent phase transition compared to thick Pd films.[11–13] These unique characteristics are considered to be derived from substrate clamping, or substrate constraint.[11,14–18] The main effect of substrate clamping is the suppression of in-plane expansion. Thus, when the in-plane expansion is suppressed completely, one-dimensional expansion along the out-of-plane (or the substrate normal) direction can be observed during hydrogen absorption.[19–23] Such anisotropic expansion is accompanied by large in-plane compressive stress, and, according to resent study, such stress affects the thermodynamic properties of hydrogen

[a]Author to whom correspondence should be addressed. Electronic mail: harumoto.t.aa@m.titech.ac.jp.

in films.[9,18,24,25] In light of this, there is a clear importance of the anisotropic expansion on the behavior of the metal-hydrogen system. However, although the *qualitative* descriptions of the anisotropic expansion can be found in many literatures, there remain few *quantitative* analyses on the anisotropic expansion.

In this study, employing in-situ X-ray diffractometry, the lattice strains in highly (111)-textured and normal Pd films during hydrogen absorption/desorption have been measured and we have analyzed the anisotropic expansion *quantitatively* using a proposed anisotropic expansion factor (f_{ae}). Accordingly, the hydrogen composition dependence on f_{ae} was revealed and described using a Sigmoid function-based equation. Note that since the texture of Pd films is considerably improved using the underlayer, the thickness dependence was also investigated down to 8 nm.

II. EXPERIMENTAL

A. Specimen preparation

Two types of Pd films – highly (111)-textured and normal – were prepared using sputtering deposition. An AlN(20 nm)/Pd(8 nm)/AlN(20 nm) three-layered underlayer (hereafter, denoted as APA-underlayer) was employed for preparing highly (111)-textured Pd films of thicknesses 8, 16, 24 and 48 nm. Although the APA-underlayer improves the (111) fiber-texture of Pd films deposited onto it, the diffraction intensity of the APA-underlayer is relatively small compared to the texture-improved Pd film as shown later (section III.A). The Pd/APA-underlayer film has been fabricated using a continuous sputter deposition process which improves the film texture.[26,27] In brief, using two direct current magnetron sputtering guns equipped with metallic platinum (Pd) and aluminum (Al) targets, the three-layered APA-underlayer and Pd films were deposited on a synthetic fused silica substrate. Because the two guns are discharged at the same gas conditions, the deposition is uninterrupted and incorporation of contaminants, such as oxygen atoms, into the interfaces is suppressed. The pressure before gas introduction was better than 5×10^{-5} Pa. Other details of deposition conditions are shown in Table I. The Pd film (thickness: 48 nm) without the APA-underlayer was also prepared by depositing it directly onto a synthetic fused silica substrate (denoted as Pd (48 nm)/substrate or normal Pd film). As shown in later, this film has weak (111) and (200) textures. Note that the deposition conditions are the same as those for fabricating (111)-textured Pd films.

The structure of the prepared film was confirmed using a transmission electron microscope (TEM) (JEM-3010; JEOL) operated at 300 kV. For cross-sectional observation, silicon (Si) (100) wafers with native oxide were also employed as a substrate. The cross-sectional specimen for TEM was prepared by argon ion milling. The texture of the film was measured using a normal X-ray diffractometer (radiation: Cu$K\alpha$, wavelength: 0.15418 nm).

B. In-situ XRD measurements

Figure 1 shows the experimental setup for the in-situ XRD measurements. A Bruker D8 Discover diffractometer was employed to measure (111) lattice spacings of α- and β-phases at the

TABLE I. Sputter deposition conditions for Pd films and the APA-underlayer.

	Pd deposition	AlN deposition
Target purity (%)	Pd 99.95	Al 99.99
Ar gas (sccm)	7	7
N_2 gas (sccm)	1	1
Total sputtering pressure (Pa)	0.50	0.50
Gun power supply	Direct current	Direct current
Gun voltage (V)	355	267
Gun current (mA)	15	70
Target-substrate distance (mm)	55	57
Substrate temperature	Room temperature	Room temperature
Deposition rate (nm/min.)	8.6	4.4

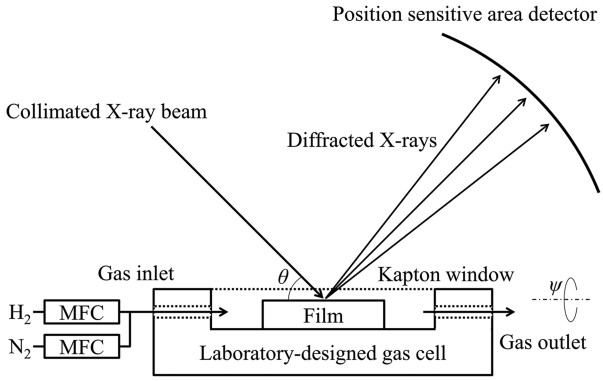

FIG. 1. Schematic illustration of the experimental setup for the in-situ XRD measurement. MFC denotes mass flow controller and is employed for preparing the N_2-H_2 gas mixture.

tilt-angles psi (ψ) = 0° and 70.5° ($d^{111}_{\psi=0°}$ and $d^{111}_{\psi=70.5°}$). Note that since the angle-difference between {111} is 70.5°, the (111)-textured film exhibits strong diffraction intensity not only at ψ = 0° but also at ψ = 70.5°. The diffractometer consists of a rotating copper anode generator, a Montel-P mirror, a laboratory-designed gas cell and a two-dimensional (2D) position sensitive Vantec-500 detector. The X-ray was generated at 50 kV, 22 mA and paralleled using the Montel-P mirror, which consists of two multilayered mirrors. The divergence of the paralleled beam is less than 0.04° in horizontal and vertical directions. The Montel-P mirror also works as a monochromator for Cu$K\alpha$, and cuts out other wavelengths such as Cu$K\beta$ X-ray. The specimen film was irradiated by a paralleled Cu$K\alpha$ X-ray beam collimated through a pinhole (diameter: 0.1 mm). It was placed at the center of the goniometer and the atmosphere around the specimen film was controlled using two mass flow controllers for hydrogen and nitrogen gases. Diffracted X-rays were collected using the Vantec-500 detector placed at 199.8 mm from the specimen. The frame size of the detector was 2048 × 2048 pixels and the size of each pixel was 68 × 68 μm^2. The data acquisition steps are shown in Fig. 2. One set of measurements consisted of 136 cycles and took about six and a half hours for each film. During the XRD measurement, 0%, 2%, 0%, 4%, 0%, 6%, 0%, 8%, 0%, 10% and 0% H_2 gases mixed with pure-N_2 were introduced sequentially. The H_2 gas profile over time is shown later (Sec. III C). All measurements were conducted at room temperature (~293 K) and atmospheric pressure.

After the measurement, line profiles were extracted from the two-dimensional frames. The backgrounds of each profile were subtracted using the profiles of the APA-underlayer or the synthetic fused silica substrate measured in the same manner. In other words, the profiles employed for profile fitting were derived only from the Pd films on the APA-underlayer or on the substrate. The peak intensity, peak position and the full width at half maximum (FWHM, or 2w) were determined by fitting the peak with a pseudo-Voigt profile. Since the incident beam contained Cu$K\alpha_1$ and Cu$K\alpha_2$, the fitting was conducted under the assumption that the peak consisted of two peaks corresponding

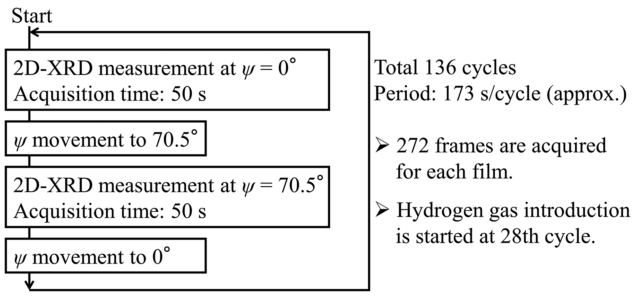

FIG. 2. Details of the measurement procedure. Note that the period of 173 s/cycle consists of two 50 s measurements and 73 s diffractometer internal processing such as ψ-angle movement.

to $K\alpha_1$ and $K\alpha_2$. All profile fittings were conducted using Mathematica (Version 9; Wolfram, Champaign, IL, USA). Note that the accuracy of the diffraction angle (2θ) and the amount of instrumental broadening of the diffractometer were confirmed using NIST SRM 640c silicon powder. The 640c powder was installed to the gas cell similarly to the in-situ measurement of the films. The diffraction profiles were acquired at $\psi = 0^\circ$ and 70.5° and the accuracy of 2θ was better than 0.04° for all ψ. The sum of this 0.04° error and the standard error of peak position during the profile fitting was adopted as a possible total error, and indicated by error bars in figures after consideration of error propagation.

C. Analyses of measured results

The measured results were first analyzed using rhombohedral distortion analysis, which can calculate the in-plane lattice strain from measured lattice spacings without any elastic constants. Thereafter, the same measured results were analyzed using diffraction stress analysis, in which in-plane stress and the strain-free lattice parameter were estimated. In addition, the hydrogen composition was calculated from the strain-free lattice parameter. Note that all analyses were conducted under the assumption that there was no stress gradient in the Pd films. This assumption is widely employed for the case of thin films.[28]

1. Rhombohedral distortion analysis

The rhombohedral distortion analysis method is based on the primitive rhombohedral cell of fcc.[29] This method can be used for films with (111) fiber-texture and stress with rotational symmetry (*i.e.* $\sigma_{11} = \sigma_{22} = \sigma_{\parallel}$ where σ_{11} and σ_{22} are in-plane stresses). The parameters inferred from the analysis are the angle (γ_r) and the lattice parameter (l_r) of the rhombohedral cell. These two parameters can be calculated from the measured lattice spacings of (111) planes at two different ψ angles, 0° and 70.5° ($d^{111}_{\psi=0^\circ}$ and $d^{111}_{\psi=70.5^\circ}$);

$$\gamma_r = \arccos\left(\frac{3{d^{111}_{\psi=0^\circ}}^2 - {d^{111}_{\psi=70.5^\circ}}^2}{3{d^{111}_{\psi=0^\circ}}^2 + {d^{111}_{\psi=70.5^\circ}}^2}\right), \tag{1}$$

$$l_r = \sqrt{\frac{3}{1+2\cos\alpha_r}}\, d^{111}_{\psi=0^\circ}. \tag{2}$$

Since the in-plane lattice spacing of (110) can be written as[29]

$$d^{110}_{\psi=90^\circ} = l_r\sqrt{2(1-\cos\gamma_r)}, \tag{3}$$

the in-plane (||) strain referenced from (110) lattice spacing of bulk Pd ($d^{110}_{\text{bulk Pd}}$) is described as

$${\varepsilon_{\parallel}}^{\circ} = \frac{d^{110}_{\psi=90^\circ} - d^{110}_{\text{bulkPd}}}{d^{110}_{\text{bulkPd}}} = \frac{l_r\sqrt{2(1-\cos\gamma_r)} - d^{110}_{\text{bulkPd}}}{d^{110}_{\text{bulkPd}}}. \tag{4}$$

The out-of-plane ($^\perp$) strain referenced from (111) lattice spacing of bulk Pd ($d^{111}_{\text{bulk Pd}}$) can be simply calculated from $d^{111}_{\psi=0^\circ}$ as

$${\varepsilon_{\perp}}^{\circ} = \frac{d^{111}_{\psi=0^\circ} - d^{111}_{\text{bulkPd}}}{d^{111}_{\text{bulkPd}}}. \tag{5}$$

(Important note: In this paper, there are two-types of strains; one-type is defined using the strain-free lattice parameter and another-type is defined using the lattice spacing of bulk Pd. To distinguish between these two strains, the strains of the latter-type are indicated using the degree symbol "°" as the above equations.)

Since Eqs. (4) and (5) contain no constants except for the lattice spacings of bulk Pd, both out-of-plane and in-plane strains can be calculated without any elastic coefficients. Note that since this rhombohedral distortion analysis method is applicable only to (111)-textured film, the in-plane strain of normal film was estimated using diffraction stress analysis instead.

2. Diffraction stress analysis and estimation of hydrogen composition

Additionally, the same measured results were also analyzed using diffraction stress analysis in order to calculate the in-plane stress ($\sigma_{\parallel}$) and the strain-free lattice parameter (a_{sf}). Although an anisotropic grain interaction is known to be present in thin Pd films,[28] the simplest grain-interaction model was employed, *i.e.* Reuss and Voigt grain-interaction models[29–35] for (111)-textured film, and Eshelby–Kröner model[35–39] for normal film. This was because there were not enough measured results to discuss the anisotropic grain interaction.

Accordingly, the strain of (111) lattice at the tilt angle ψ can be described as

$$\varepsilon_{\psi}^{111} = \frac{d_{\psi}^{111} - a_{sf}/\sqrt{3}}{a_{sf}/\sqrt{3}} = \left(2S_1^{111} + \tfrac{1}{2}S_2^{111}\sin^2\psi\right)\sigma_{\parallel} \tag{6}$$

where d_{ψ}^{111} is the (111) lattice spacing at ψ and a_{sf} is a strain-free lattice parameter. When two (111) lattice spacings at $\psi = 0^\circ$ and 70.5° ($d_{\psi=0^\circ}^{111}$ and $d_{\psi=70.5^\circ}^{111}$) are measured, the strain-free lattice parameter and the in-plane stress can be calculated from Eq. (6) as

$$a_{sf} = \sqrt{3}\left(\left(\frac{9S_1^{111}}{4\frac{1}{2}S_2^{111}} + 1\right)d_{\psi=0^\circ}^{111} - \frac{9S_1^{111}}{4\frac{1}{2}S_2^{111}}d_{\psi=70.5^\circ}^{111}\right), \tag{7}$$

$$\sigma_{\parallel} = \frac{1}{2S_1^{111}}\left(\frac{d_{\psi=0^\circ}^{111}}{a_{sf}/\sqrt{3}} - 1\right). \tag{8}$$

Note that the approximation of $\sin^2 70.5^\circ = 8/9$ is employed.

The constants S_1^{111} and $\frac{1}{2}S_2^{111}$ are diffraction elastic constants for 111 reflection and have texture dependence. Table II summarizes the calculated diffraction elastic constants for (111)-textured and normal Pd films. These constants are calculated using following single-crystal elastic compliances in Ref. 40: $s_{11} = 13.744$ TPa^{-1}, $s_{12} = -5.995$ TPa^{-1} and $s_{44} = 14.035$ TPa^{-1} for Pd. $s_{11} = 12.923$ TPa^{-1}, $s_{12} = -5.507$ TPa^{-1} and $s_{44} = 15.760$ TPa^{-1} for $PdH_{0.66}$. In the case of (111)-textured film, S_1^{111} and $\frac{1}{2}S_2^{111}$ can be described simply as (1/3) s_{11} + (2/3) s_{12} − (1/6) s_{44} and (1/2)s_{44}, respectively.[29–35] In contrast, S_1^{111} and $\frac{1}{2}S_2^{111}$ for normal film are calculated by solving equations in Ref. 39. Since the hydrogen composition dependence on the elastic compliances could not be found in literature, the assumption that the diffraction elastic constants of α- and β-phases are the same as pure-Pd and $PdH_{0.66}$, respectively, was applied in the following.

Employing the strain-free lattice parameter calculated from Eq. (7), the hydrogen composition (x_H), defined as the H/Pd atomic ratio, is estimated using the following equation[18,41]

$$\frac{a_{sf} - a_{\text{bulk Pd}}}{a_{\text{bulk Pd}}} = \alpha_H x_H = 0.061 x_H \tag{9}$$

where α_H is a (linear) expansion coefficient due to hydrogen incorporation. The value of 0.061 is the average of 0.063 in the literature[18,41] and 0.059, which is estimated from Vegard law between pure-Pd and $PdH_{0.603}$.[1] Note that this equation is valid at both α- and β-phases. Also, since the strain-free lattice parameter is the lattice parameter at the *stress-free* state, the hydrogen composition can be estimated without the influences of the stress, its relaxation and the grain boundaries. The $a_{\text{bulk Pd}}$ denotes the bulk lattice parameter of pure-Pd (0.389019 nm[42]).

TABLE II. Diffraction elastic constants for (111)-textured and normal Pd films. These are calculated using single-crystal elastic compliances in Ref. 40.

	Grain-interaction model employed for calculation	S_1^{111}(TPa^{-1})	$\frac{1}{2}S_2^{111}$(TPa^{-1})
(111)-textured Pd film	Reuss and Voigt[29–35]	−1.754	7.018
(111)-textured $PdH_{0.66}$ film	Reuss and Voigt[29–35]	−1.991	7.880
Normal Pd film	Eshelby–Kröner[35–39]	−2.297	8.645
Normal $PdH_{0.66}$ film	Eshelby–Kröner[35–39]	−2.491	9.382

III. RESULTS AND DISCUSSION

A. Film structure

The texture of the prepared films was confirmed using normal θ-2θ XRD measurements (Fig. 3). It is clear that the Pd(48 nm)/substrate has weak (111) and (200) textures, as both 111_{Pd} and 200_{Pd} peaks were detected. In contrast, the Pd film on the APA-underlayer is highly (111)-textured, since a strong 111_{Pd} peak was observed. Note that the APA-underlayer exhibits no peak at around 111_{Pd} and therefore does not affect measurements on the 111_{Pd} peak of the texture improved Pd(x nm) film deposited on it.

Figure S1 in the supplementary material shows 111 pole figures of prepared films. It is clear that Pd films on the APA-underlayer are almost full (111) fiber-texture with the rotational symmetry, since the strong 111 pole is observed at the center and the ring at ψ = ~70°. Table S1 summarizes the pole widths at the center and they were ~2° at half-width at half maximum. According to Ref. 34, such films can be analyzed under the assumption that the film is ideal (111) fiber-texture. The 111 pole figure of the Pd(48 nm)/substrate indicates that the film has a weak (111) texture. However, this film should also have (200) texture, since the ring is observed at ψ = ~59°. Thus, the film has weak (111) and (200) textures and we analyze using the Eshelby–Kröner model. It should be noted that, according to Welzel et al.,[28] the analyzed result by the Eshelby–Kröner model is very closed to the one by the state-of-the-art effective grain-interaction model, even in the case of the weak (111) fiber-texture.

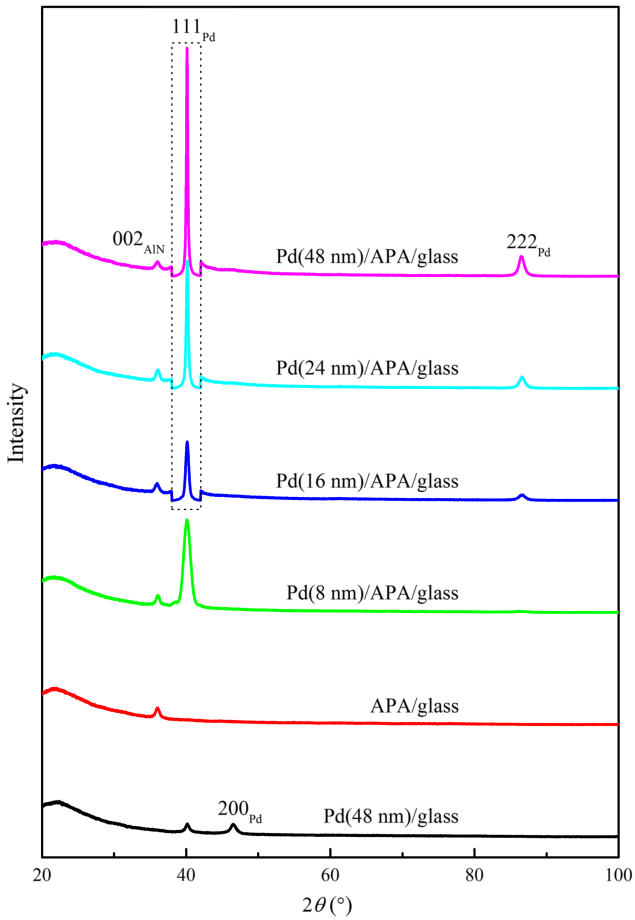

FIG. 3. XRD profiles of (111)-textured Pd(x nm)/APA-underlayer/substrate and normal Pd(48 nm)/substrate. Note that the APA-underlayer is abbreviated as APA. In the dashed line rectangle, the diffraction intensity is multiplied by 1/10.

The rotational symmetry in the in-plane stress was investigated using the in-plane rotation angle (ϕ) dependence on the (111) lattice spacing at $\psi = 70.5^\circ$ (Fig. S2 in the supplementary material). Since the deviation is less than the error range, the validity of the assumption "$\sigma_{11} = \sigma_{22} = \sigma_{\parallel}$" is confirmed.

In the case of Pd films deposited on the APA underlayer, the layer structure was further investigated using cross-sectional TEM. The bright-field (BF) image of the Pd(8 nm)/APA-underlayer/substrate is shown in Fig. 4(a). The designed film structure consisting of the Pd film and APA-underlayer was confirmed. The thicknesses of each layer measured from TEM images, Pd(7.9 nm)/AlN(17.8 nm)/Pd(7.8 nm)/AlN(19.1 nm)/SiO_x(0.7 nm)/Si wafer, were in good agreements with the designed thicknesses. The dark-field (DF) image and the selected area electron diffraction (SAED) pattern demonstrated that the Pd film on the APA-underlayer had (111) texture and the upper AlN in the APA-underlayer was in c-axis preferred orientation while other layers were polycrystalline (Figs. 4(b) and (c)). It should be noted that although all layers are served for acquiring SAED, the diffraction rings of bottom two layers are submerged in background due to the strong 111_{Pd} and 002_{AlN} spots derived from the upper two layers. The high-resolution TEM (HRTEM) image further confirmed (111) texture of the Pd film on the APA-underlayer (Fig. 4(d)) and no texture of the Pd layer in the APA-underlayer (Fig. 4(e)). According to the (111) lattice image of Fig. 4(d), the crystal size along the substrate normal, or the vertical grain size, of Pd is almost equal to the thickness of the Pd film (8 nm). The roughnesses of the interfaces between Pd and AlN layers are around 2 nm. Since the lattice fringes of Pd were connected to that of AlN in some parts, local-epitaxial growth at the interface took place.

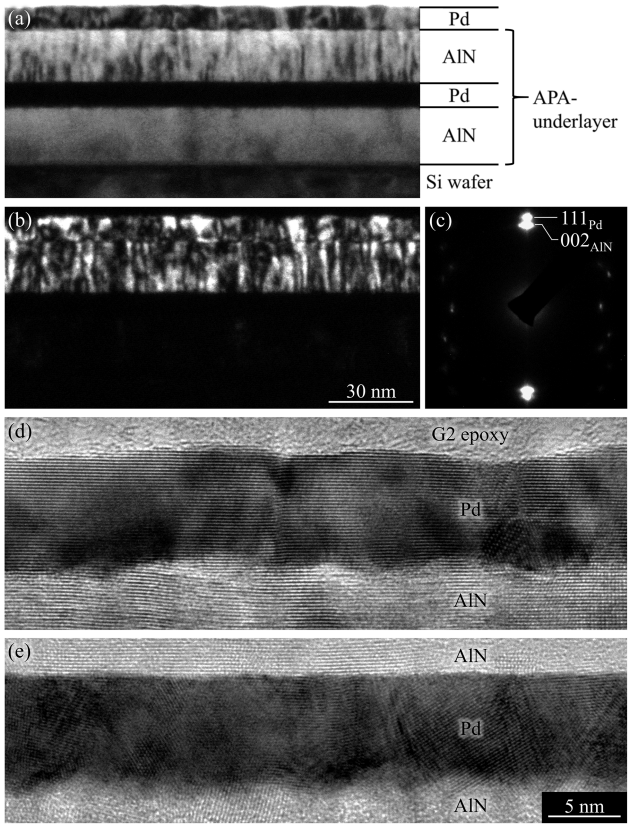

FIG. 4. Cross-sectional TEM observation of (111)-textured Pd(8 nm)/APA-underlayer/substrate. (a) and (b) are BF and DF images at the same position. (c) is the corresponding SAED pattern. The DF image was acquired using 111_{Pd} and 002_{AlN} spots normal to the substrate. (d) HRTEM image of Pd(8 nm) film deposited on the APA-underlayer. (e) HRTEM image of Pd (8 nm) layer in the APA-underlayer. According to lattice fringes in HRTEM images, the Pd film on the APA-underlayer is highly (111) fiber-textured while Pd layer in the APA-underlayer has no texture.

In summary, the Pd film on the APA-underlayer was highly (111) fiber-textured, while the Pd film deposited directly on the substrate had weak (111) and (200) textures. The APA-underlayer is an ideal underlayer from the viewpoint of diffractometry since there is no intensity around the 111_{Pd} peak position in the diffraction profile. Based on these results, we used the prepared highly (111)-textured Pd films deposited on the APA-underlayer and the normal Pd film to conduct the in-situ XRD investigation.

B. In-situ XRD measurements

Typical in-situ XRD profiles, shown in Fig. 5, indicate the formation of β-phase in the emergence of a new peak at around 38.5° when $\psi = 0°$, and 39° when $\psi = 70.5°$ (Note: the peak position difference is related to the in-plane stress and discussed in the next section).

It is clear that the hydrogen concentration for the β-phase formation exhibits thickness dependence: the thicker film tends to form β-phase while the thinner film has a resistance against hydride formation (Figs. 5(a)–(d)). For example, in the case of 8% H_2, the 48 nm-thick Pd film is almost entirely in β-phase, the 24 and 16 nm-thick Pd films are a composite of α- and β-phases, and the 8 nm-thick Pd film is mainly in α-phase. This result is in agreement with the literature that thinner Pd films exhibit less resistivity change while thicker Pd films show large change due to β-phase formation.[10]

Also, in comparison with the normal Pd(48 nm)/substrate, it can be concluded that (111)-texture also suppresses the formation of β-phase (Figs. 5(d) and (e)). In the case of 4% H_2, the main phase of (111)-textured film remains in α-phase while the normal film has already transformed into β-phase. These thickness and texture dependences can be explained by substrate clamping.[11,15–18]

Figure 6 shows a typical reciprocal space map during hydrogen introduction. The observed spots at the center are 111 reflections of α- and β-phases. The intensity distributions of both α- and β-phases were in spots rather than rings and follow the line of $q_y = 0$, indicating that the (111) texture is retained during α-to-β phase transformation. In addition, since the spot width along the q_y direction of β-phase is almost equal to one of α-phase, we see that the in-plane crystal size is also retained. Similar retainment was also observed in β-to-α transformation (not shown). Thus, in the case of textured film, the formation of hydride phase and subsequent recovery of metallic phase took place while retaining both the film texture and the in-plane crystal size. This may be related to the coherent phase transition,[11,13,16] however, the details are still under investigation.

C. Anisotropic lattice expansion due to substrate clamping

To further investigate the process, the center positions, FWHM and peak intensities of α- and β-phases were estimated using peak profile fitting. The calculated peak profiles are shown as red lines in Fig. 5 and show good agreement with the measured profiles. The fitting and the analysis results are summarized in Fig. 7 (in the supplementary material, the undivided version of this figure can be found).

The peak intensities (peak heights) of α- and β-phases clearly demonstrated that the hydride formability has the thickness and texture dependences discussed in the previous section (first row of Fig. 7). For example, the (111)-textured 8 nm-thick Pd film diffraction pattern exhibits no β-phase intensity at up to 6% H_2 while that of the (111)-textured 48 nm-thick Pd film shows β-phase intensity from 4% H_2. In addition, since the XRD intensity of the final hydrogen lading stage is slightly larger than that of the initial loading stage, the crystallinity and/or the texture of the film should be improved by hydrogen absorption and subsequent desorption. Since hydrogen absorption/desorption cycles are known to result in crystallinity degradation, this intensity increase could be explained by the texture improvement. Similar texture improvement has been already reported by Gremaud *et al.*[16]

The FWHM of the peak at $\psi = 0°$ corresponds to crystal size along the out-of-plane direction (or the vertical grain size) and non-uniform strain (second row of Fig. 7). Although it is difficult to treat these two effects separately, the following is clear: when the film is in a single-phase of α- or β-phase, the vertical grain size is large and the non-uniform strain is small because the FWHM is small. When the film is in a mixture of α- and β-phases, the vertical grain size is small and/or the non-uniform strain is large since the FWHM is larger than the single-phase case. Hence, it can

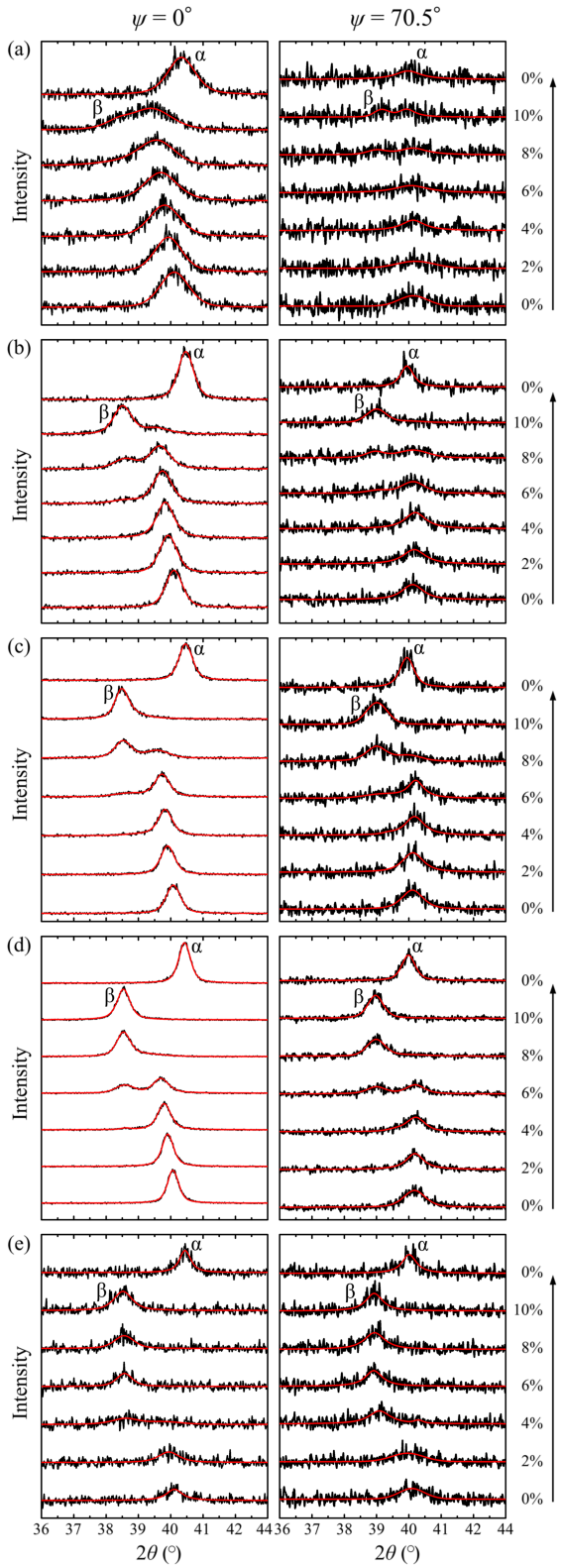

FIG. 5. Typical in-situ XRD results of (111)-textured Pd(x nm)/APA-underlayer/substrate: (a) x = 8, (b) x = 16, (c) x = 24 and (d) x = 48. The results of normal Pd(48 nm)/substrate are also shown in (e). The black lines denote the measured profiles and the red lines are the calculated profiles during the profile fittings. The left and right columns correspond to profiles at $\psi = 0°$ and 70.5°, respectively. The α and β indicate 111 peaks of α- and β-phases.

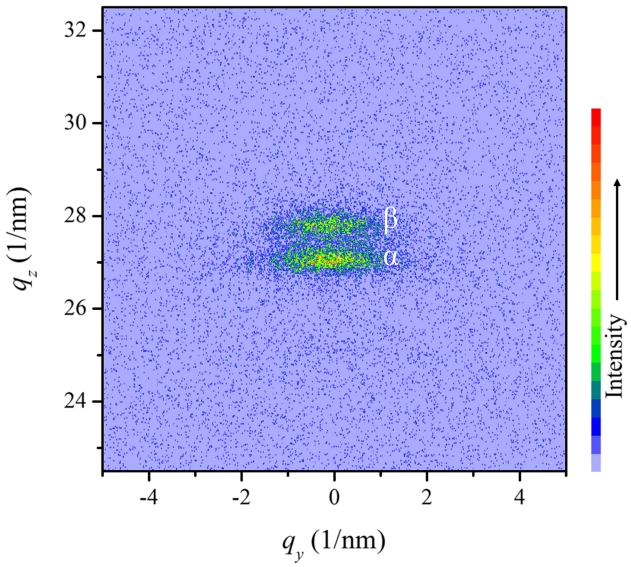

FIG. 6. Reciprocal space map around 111 diffraction spots of Pd(24 nm)/APA-underlayer/substrate during 8% hydrogen introduction. Note that q_y and q_z denote reciprocal space vectors along in-plane and out-of-plane directions, respectively. The α and β in the figure indicate 111 spots of α- and β-phases.

be concluded that, during the β-phase formation, the film is non-uniformly strained and the vertical grain size is decreased. However, once α-phase transforms to β-phase completely, the non-uniform strain in the film disappears and the vertical grain size returns to the initial one.

According to strain along out-of-plane and in-plane directions (third and fourth rows of Fig. 7), the strain before hydrogen introduction was almost equal to 1 for any direction and thickness, indicating that stress in the films was almost zero and lattices consisted of Pd with a lattice parameter equal to the bulk one. After the hydrogen introduction, lattice expansion occurred, dividable into two stages: an initial stage before β-phase formation and second one during β-phase formation.

During the initial stage of hydrogen absorption, the lattice expansion occurred mainly along the out-of-plane direction (up to 1% expansion) with almost zero expansion/shrinkage along the in-plane direction (compare third row to fourth row of Fig. 7). This anisotropic expansion was observed in all films. This clearly demonstrates that the lattice expansion in the initial stage was one-dimensional. After replacing the 2% hydrogen gas with 100% nitrogen gas, the lattice expansion was halted and the strain returned to 1. Thus, within this initial stage, the lattice expansion and shrinkage can be considered to be a one-dimensional reversible process and no plastic deformation takes place.

At the start of second stage, the film is a combination of hydride β-phase and metallic α-phase, before finally transforming into β-phase completely. The formation of β-phase was observed as the lattice expanded in both out-of-plane and in-plane directions, indicating the decrease of the out-of-plane anisotropy in β-phase. The measured 3–4% expansion was reasonable from the viewpoint of hydride formation, since the lattice constant difference between bulk Pd and $PdH_{0.6}$ is known at 3.5%.[1,41] In detail, the observed out-of-plane expansion was ~4% and slightly larger than for in-plane (~3%). This can be explained by the in-plane compressive stress which is discussed in the next section. In the α-phase, in addition to the lattice expansion along the out-of-plane direction, the lattice *shrinkage* along the in-plane direction was observed in this second stage. This observation is different from the initial stage (*i.e. no* expansion/shrinkage along in-plane direction). This lattice shrinkage in the α-phase is considered to be derived from the formation of the β-phase of which in-plane expansion is relatively large (~2-3%). The observed large in-plane stress supports this consideration. Once β-phase forms, the hydrogen absorption-desorption reaction becomes irreversible. The strain after hydrogen desorption cannot return to zero, indicating that the plastic deformation, such as an introduction of misfit dislocations at the film/(substrate or underlayer) interface,[11,13,16] takes place during the β-phase formation. In fact, the out-of-plane strain after recovering α-phase reached negative 0.5–1%, while the in-plane strain was positive. This strain could

be considered to be an elastic deformation due to the in-plane tensile residual stress deriving from the plastic deformation during α-to-β transformation and the subsequent large shrinkage during β-to-α transformation.

According to these observations, we conclude the following: in the initial stage, the reversible lattice expansion/shrinkage occurred only along the out-of-plane direction, while there was no expansion/shrinkage along the in-plane direction. This anisotropic lattice expansion, or one-dimensional expansion, indicates that no plastic deformation took place at this initial stage. During the second stage, the formation of β-phase was observed through large expansions around 3–4% along both out-of-plane and in-plane directions resulting in irreversibility. During the formation of β-phase, plastic deformation occurred and it results in the decrease of the out-of-plane anisotropy. This indicates that the anisotropic expansion has a hydrogen composition dependence. After returning to its metallic lattice (α-phase), there was large in-plane tensile residual stress derived from the plastic deformation during α-to-β transformation and the subsequent lattice shrinkage during β-to-α transformation.

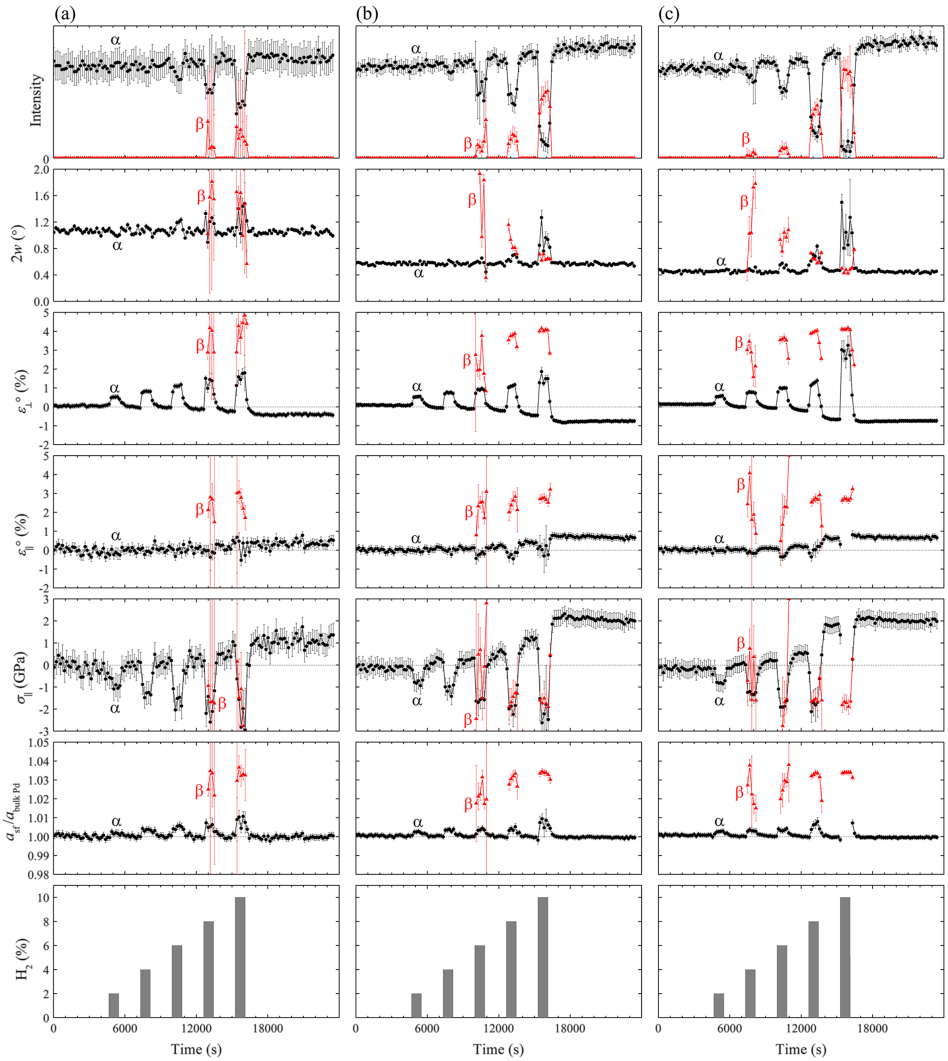

FIG. 7. Analyzed results on XRD profiles of (111)-textured Pd(x nm)/APA-underlayer/substrate: (a) x = 8, (b) x = 16, (c) x = 24 and (d) x = 48. The results of normal Pd(48 nm)/substrate are also shown in (e). The peak intensity at $\psi = 0°$ (first row), FWHM ($2w$) of the peak at $\psi = 0°$ (second), out-of-plane strain ($\varepsilon_\perp$) (third), in-plane strain ($\varepsilon_\parallel$) (fourth), in-plane stress ($\sigma_\parallel$) (fifth), strain-free lattice parameter (a_{sf}) (sixth), and hydrogen gas concentration introduced to the cell (seventh) are plotted against time. Note that the strain-free lattice parameter is normalized using the bulk lattice parameter of pure-Pd ($a_{\text{bulk Pd}}$), even in the case of β-phase. In the supplementary material, the undivided version of this figure can be found.

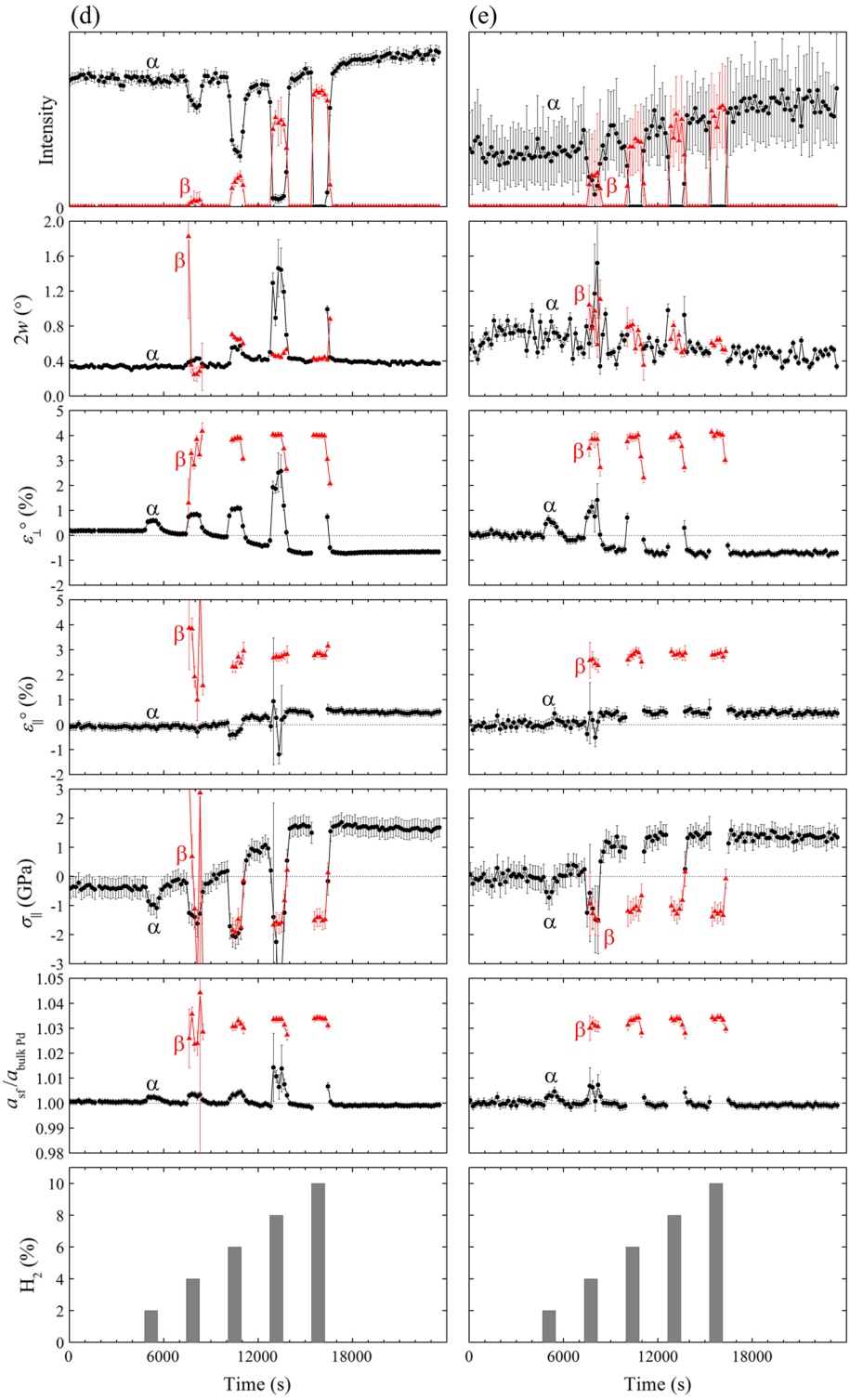

FIG. 7. (*Continued.*)

D. In-plane stress and lattice parameter changes during hydrogen absorption and desorption

Following this, the in-plane stress in the films and the strain-free lattice parameters of α- and β-phases were calculated using diffraction stress analysis (fifth and sixth rows of Fig. 7). Note that

the strain-free lattice parameters have been normalized using one of the bulk pure-Pd (0.389019 nm), even in the case of β-phase.

The in-plane stress before hydrogen introduction was almost zero (more specifically, although within error, there was slight compressive stress in the films possibly attributed to the atomic peening effect[43]) (fifth row of Fig. 7). The normalized strain-free lattice parameter was close to 1 (sixth row of Fig. 7).

The hydrogen incorporation was observed in both large in-plane compressive stress (up to a few GPa) and the increase of the strain-free lattice parameter. The observed large in-plane compressive stress exhibited good agreement with that measured by substrate curvature in the literature.[13–15,18] During the initial stage, these two parameters returned to initial values after the hydrogen introduction was cut-off, indicating reversible process. These are good agreement with the discussion in the previous section.

The formation of β-phase took place under the same in-plane stress that α-phase receives, since the in-plane stress in β-phase was almost equal to the stress in α-phase (in the figure, this is observed as an overlap of black (corresponding to α-phase) and red (to β-phase) lines). During this second stage, the reaction becomes irreversible, since the in-plane stress does not recover its initial value and there remains large tensile stress. This tensile stress was considered to be derived from the lattice shrinkage during recovery of α-phase and indicated that plastic deformation occurred during the α-to-β phase transformation. Note that, although the lattice was elastically deformed due to the in-plane tensile stress, the Pd lattice recovered its own lattice parameter after hydrogen desorption.

E. Quantitative description of anisotropic expansion

It was shown in the previous sections that the anisotropic expansion was almost perfect during the initial stage (before the β-phase formation) and its out-of-plane anisotropy is weakened during the β-phase formation due to plastic deformation, such as the formation of misfit dislocation at the film/(substrate or underlayer) interface. This indicated that the anisotropic expansion had a hydrogen composition dependence and was suitable for quantitative analysis. Accordingly, in this section, we introduce an anisotropic expansion factor and investigate the hydrogen composition dependence.

Since the substrate clamping is frequently discussed with out-of-plane strain,[15,18,20,22,24] we chose to introduce the anisotropic expansion factor into the equation for the out-of-plane strain. If the film is allowed to expand freely (three-dimensionally), the strain along the out-of-plane direction can simply be described by the same equation as Eq. (9):

$$\varepsilon_{\perp}{}^{\circ} = \alpha_{\mathrm{H}} x_{\mathrm{H}} \tag{10}$$

If no in-plane expansion takes place due to the substrate clamping, the in-plane compressive stress which cancels the in-plane expansion ($\alpha_{\mathrm{H}} x_{\mathrm{H}}$) is generated by substrate clamping and such compressive stress results in an additional out-of-plane expansion ($\varepsilon_{\perp}{}^{\mathrm{additional}\,\circ}$).[15,18,20,22,24] When we employ the biaxial Poisson's ratio $\nu_{\mathrm{bi}} = (-\varepsilon_{\perp}/\varepsilon_{\parallel})$,[44] this additional out-of-plane expansion can be simply expressed as the following:

$$\varepsilon_{\perp}{}^{\mathrm{additional}\,\circ} = -\nu_{\mathrm{bi}} \varepsilon_{\parallel}{}^{\circ} = -\nu_{\mathrm{bi}} \times (-\alpha_{\mathrm{H}} x_{\mathrm{H}}) = \nu_{\mathrm{bi}} \alpha_{\mathrm{H}} x_{\mathrm{H}}. \tag{11}$$

Accordingly, the total observed out-of-plane expansion is a sum of Eqs. (10) and (11),

$$\varepsilon_{\perp}{}^{\circ} = \alpha_{\mathrm{H}} x_{\mathrm{H}} + \varepsilon_{\perp}{}^{\mathrm{additional}\,\circ} = \alpha_{\mathrm{H}} x_{\mathrm{H}} + \nu_{\mathrm{bi}} \alpha_{\mathrm{H}} x_{\mathrm{H}} = (1 + \nu_{\mathrm{bi}}) \alpha_{\mathrm{H}} x_{\mathrm{H}}. \tag{12}$$

Here, considering the difference between the equation for the one-dimensional expansion (Eq. (12)) and the equation for the three-dimensional expansion (Eq. (10)), we introduce an anisotropic expansion factor f_{ae} to describe the anisotropic expansion of the lattice quantitatively and rewrite Eq. (12) as follows:

$$\varepsilon_{\perp}{}^{\circ} = (1 + f_{\mathrm{ae}} \nu_{\mathrm{bi}}) \alpha_{\mathrm{H}} x_{\mathrm{H}}. \tag{13}$$

Clearly, $f_{\mathrm{ae}} = 0$ indicates the three-dimensional expansion while $f_{\mathrm{ae}} = 1$ corresponds to the one-dimensional expansion. Note that since the biaxial Poisson's ratio for (111)-textured Pd film is known to be 1.01,[44] $(1 + f_{\mathrm{ae}} \nu_{\mathrm{bi}}) \alpha_{\mathrm{H}}$ for $f_{\mathrm{ae}} = 1$ is equal to 0.123 and almost twice the value of 0.061

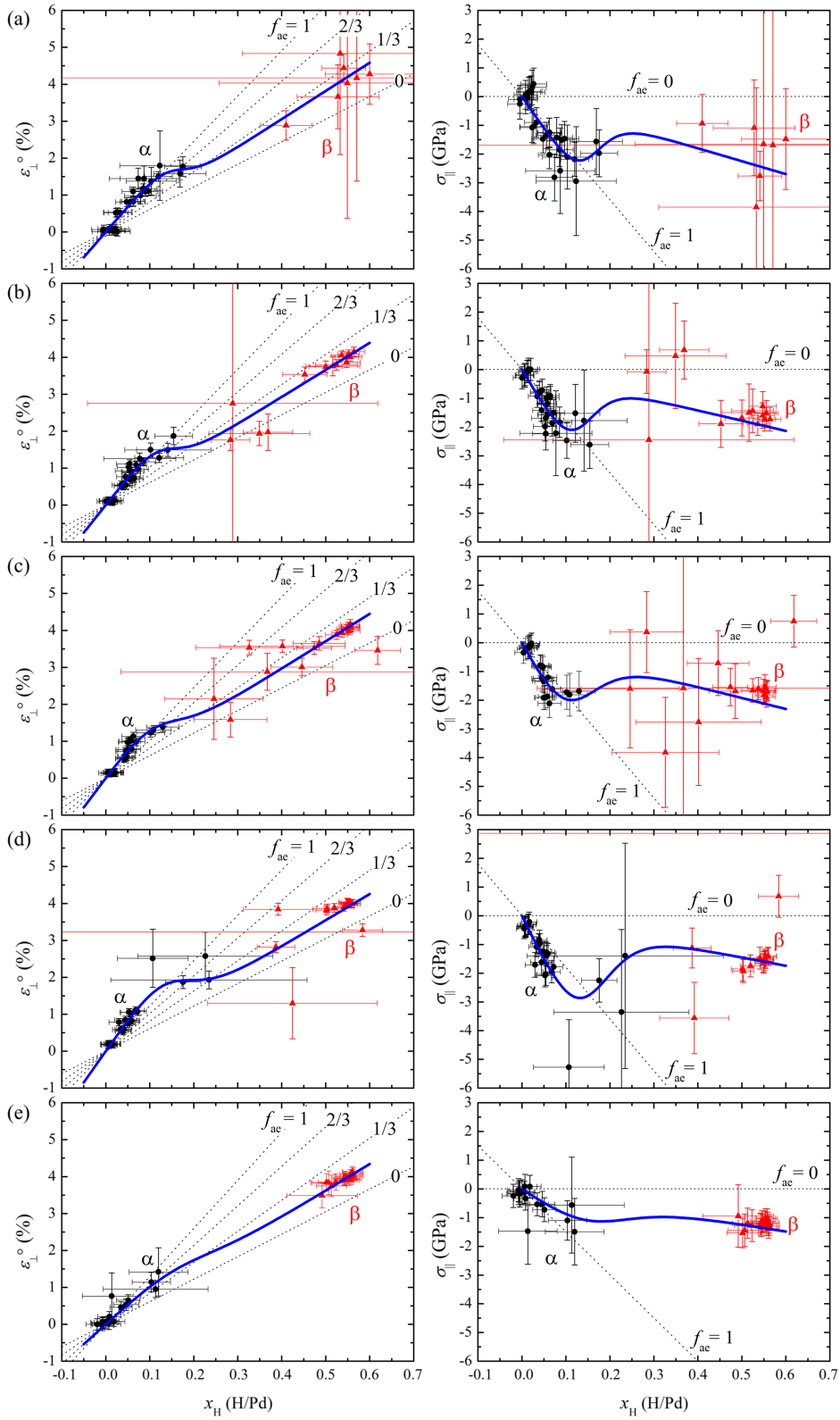

FIG. 8. Hydrogen composition dependences on out-of-plane strain and in-plane stress in (111)-textured Pd(x nm)/APA-underlayer/substrate during hydrogen introduction: (a) x = 8, (b) x = 16, (c) x = 24 and (d) x = 48. The results of normal Pd(48 nm)/substrate are also shown as (e). The blue solid lines in figures are calculated from the hydrogen composition dependent f_{ae} described by the Sigmoid function-based equation (Eq. (14)). The thin dotted lines indicate the calculated results under the assumption that f_{ae} is constant.

for $f_{ae} = 0$. In the case of normal Pd film, the ratio is 1.13 (details in Appendix) and $(1 + f_{ae}\nu_{bi})\alpha_H$ for $f_{ae} = 1$ is equal to 0.130.

The left column of Fig. 8 shows the hydrogen composition versus the out-of-plane strain during hydrogen introduction. Using Eq. (13), the lines of $f_{ae} = 0$, 1/3, 2/3, and 1 are plotted on the figures. It is clear for the (111)-textured Pd(x nm)/APA-underlayer/substrate that the f_{ae} is slightly greater than 1 at α-phase and less than 1/3 at β-phase. In the case of the normal Pd(48 nm)/substrate, f_{ae} is around 2/3 at α-phase and less than 1/3 at β-phase.

Considering the two stages in hydrogen absorption, the following Sigmoid function-based equation is considered to describe the hydrogen composition dependence on the anisotropic expansion factor:

$$f_{ae} = \frac{f_\alpha - f_\beta}{1 + \exp\left(s_c(x_H - x_c)\right)} + f_\beta. \tag{14}$$

Figure 9 shows the schematic drawing of this equation. The f_α and f_β are the anisotropic expansion factors at low (α-phase) and high (β-phase) hydrogen composition. The x_c and s_c describe the transition center and transition rate factor from f_α to f_β. Note that although f_β may exhibit the hydrogen composition dependence, it was treated as a constant. This is because the composition dependence on f_β should be relatively small, since we cannot find a trace of it, such as a saturation of out-of-plane expansion at β-phase, in Fig. 8. It was also considered that even if more accurate diffractometer was employed, it might be difficult to observe such small composition dependence, since the large plastic deformation was already introduced to the film/substrate interface at the α-to-β transformation.

Using this equation, the measured results were analyzed and the best-fit parameters with standard errors are shown in Fig. 10. Also, the calculated $\varepsilon_\perp$ curves using these parameters are added to Fig. 8 (blue solid lines). The calculated curves exhibit good agreement with the experimental plots.

The anisotropic expansion factor at low hydrogen composition (f_α) of Pd films on the APA-underlayer is slightly larger than 1, indicating that the out-of-plane lattice expansion at low hydrogen composition is larger than the case for no in-plane expansion (first row of Fig. 10). Thus, the expansion at this stage is an anomalous one-dimensional expansion. Similar anomalous expansion in Nb film has been reported previously.[19,20] At present, we cannot directly explain the observed anomalous expansion. However, since the simple Pd(48 nm) film exhibits a reasonable f_α, this anomalous expansion may be related to the (111)-texture and/or the local-epitaxial growth at the Pd(x nm)/APA-underlayer interface. The anisotropic expansion factor at high hydrogen composition (f_β) does not exhibit thickness and texture dependences with a value around 0.2. This demonstrates that although the out-of-plane anisotropy becomes weak during β-phase formation, the film remains adhere even after the completion of the α-to-β phase transformation and the influences of thickness and texture on the anisotropy can be ignored. The parameter x_c is around 0.15 and does not exhibit thickness or texture dependences (second row of Fig. 10). This parameter may be related to composition where

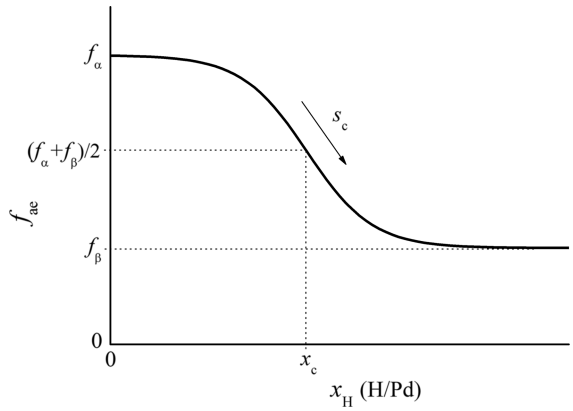

FIG. 9. Schematic illustration of the Sigmoid function-based Eq. (14) for describing hydrogen composition dependence on the anisotropic expansion factor.

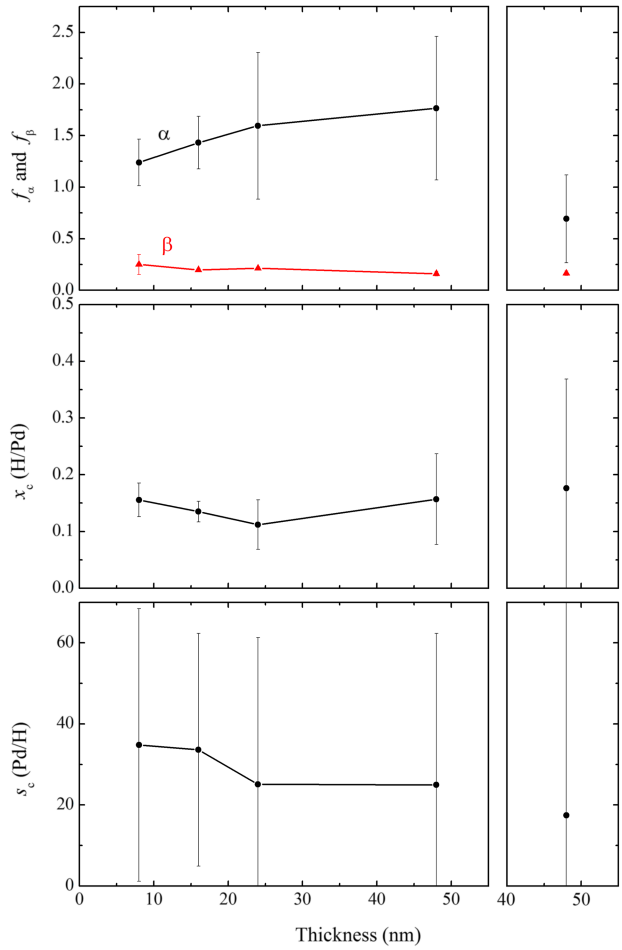

FIG. 10. Best-fit parameters for describing the hydrogen composition dependence on the anisotropic expansion factor. The left column shows fitting results of (111)-textured Pd(x nm)/APA-underlayer/substrate while the right column is that of normal Pd(48 nm)/substrate.

α- and β-phases coexist or a solubility limit of the α-phase. Regarding s_c (third row of Fig. 10), since the errors of the parameter are relatively large, no discussion is carried out at this moment.

Note that we cannot find any thickness dependence on f_{ae}, even though an obvious thickness dependence on β-phase formation is observed in in-situ XRD profiles. This suggests that the anisotropic expansion factor is related purely to the film/(substrate or underlayer) interface. The observed thickness dependence on the β-phase formation should be understood in terms of the effect of in-plane stress on thermodynamic properties[18,24,25] rather than by the interfacial effect (f_{ae}) directly.

Next, the in-plane stress is estimated from the hydrogen composition dependence on the anisotropic expansion factor. Referring to Eq. (6), the relation between the out-of-plane (*i.e.* $\psi = 0$) strain and the in-plane stress can be described as

$$\varepsilon_\perp = \varepsilon^{111}_{\psi=0^\circ} = 2S_1^{111}\sigma_\parallel. \tag{15}$$

Thus, the in-plane stress originating from the additional out-of-plane expansion ($= f_{ae}\nu_{bi}\alpha_H x_H$) can be expressed as:

$$\sigma_\parallel = \frac{\nu_{bi}\alpha_H}{2S_1^{111}} f_{ae} x_H. \tag{16}$$

When we employ the diffraction elastic constants for pure-Pd, the proportional coefficient $\frac{\nu_{bi}\alpha_H}{2S_1^{111}}$ is equal to −18 GPa for (111)-textured film and −15 GPa for normal film. Note that the calculated

coefficient for (111)-textured film agrees with the value reported by Wagner *et al.*[18] (details in Appendix).

The right column of Fig. 8 shows the relation between the hydrogen composition and the in-plane stress. Using Eq. (16), the lines of $f_{ae} = 0$ and 1 are plotted as thin dotted lines and the curves calculated from the Sigmoid function-based equation are shown in blue solid lines. It is clear that the in-plane compressive stress increases linearly at low hydrogen composition, however its linearity is lost at around $x_H = 0.1$ or $\sigma_{\parallel} = 2$ GPa. After this points, the experimental plots converge at $(x_H, \sigma_{\parallel}) \approx (0.55, 1.5\ \text{GPa})$. This indicates linear stress increase at the low x_H and stress relaxation at high x_H. The constant f_{ae} lines cannot explain these phenomena. In contrast, the blue solid curves, which are based on the Sigmoid function-based f_{ae}, can estimate stress relaxation during hydride formation and exhibits good agreement with the experimental plots. On closer inspection, however, there are small deviations between the curves and β-phase plots. This could be related to the difference of diffraction elastic coefficients between Pd (α-phase) and $PdH_{0.66}$ (β). The valley at around $x_H = x_c$ could be explained by the decrease of the out-of-plane anisotropy due to start of β-phase formation. The upward-convex of the calculated curves at around $x_H = 0.2$–0.4 indicates phase instability around this composition and may enhance the phase separation into α- and β-phases.

In summary, both the out-of-plane expansion and the in-plane stress curves can be estimated using the Sigmoid function-based anisotropic expansion factor and it exhibit good agreements with the measured results, containing the stress relaxation through the plastic deformation.

IV. SUMMARY

The highly (111) fiber-textured Pd(8, 16, 24, 48 nm) films deposited on the APA-underlayer and the normal Pd(48 nm) film were prepared and in-situ XRD measurements during hydrogen absorption/desorption conducted using the diffractometer equipped with the two-dimensional position sensitive detector. The (111) lattice spacings at $\psi = 0^\circ$ and 70.5° were measured and analyzed using rhombohedral distortion analysis and diffraction stress analysis methods.

The analysis results demonstrated that, at the initial stage of hydrogen absorption (*i.e.* before hydride formation), the lattice expansion during hydrogen absorption occurs only along the out-of-plane direction. This anisotropic lattice expansion, or one-dimensional expansion, originates from the substrate clamping. The expansion can be solved after cutting-off the hydrogen introduction to recover the initial state, indicating that the absorption at this stage can be treated as one-dimensional elastic deformation and is not accompanied by plastic deformation.

During the second stage of hydrogen absorption, β-phase forms under the same in-plane compressive stress that α-phase receives. Once β-phase formation occurs, the expansion is no longer one-dimensional. Since in-plane tensile stress is observed after recovery of the metallic lattice, plastic deformation, which results in the decrease of the out-of-plane anisotropy, is seen to occur during the β-phase formation.

Hence, a clear hydrogen composition dependence on the out-of-plane anisotropy is observed. In view of this, the factor f_{ae} is introduced to treat the anisotropic expansion quantitatively and a Sigmoid function-based equation is employed for describing hydrogen composition dependence on f_{ae}. The out-of-plane strain and the in-plane stress estimated from this equation exhibit good agreement with the experimental results. The fit results demonstrated that difference in film texture results in the variation of f_{α}, the anisotropic expansion factor at low hydrogen composition. In contrast, difference in film thickness results in almost no change to f_{ae}. Thus, the observed thickness dependence on the β-phase formation should be understood in terms of the effect of the in-plane stress on thermodynamic properties. It should be noted that, in the case of Pd films on the APA-underlayer, f_{ae} is slightly larger than 1 at low hydrogen composition, indicating an anomalous one-dimensional expansion at α-phase.

SUPPLEMENTARY MATERIAL

See supplementary material for the details of film texture and the undivided version of Fig. 7.

ACKNOWLEDGMENTS

This research was supported by Grants-in-Aid for Scientific Research (KAKENHI) (Nos. 25870772 and 16K14372) from the Japan Society for the Promotion of Science (JSPS). The authors thank Mr. Y. Suzuki and Mr. H. Iida, Division of Materials Analysis O-okayama, Tokyo Institute of Technology, for their support.

APPENDIX : CALCULATION OF BIAXIAL POISSON'S RATIO

According to Eq. (6), strains along the out-of-plane and in-plane directions can be described as

$$\varepsilon_{\perp} = \varepsilon^{111}_{\psi=0^\circ} = 2S_1^{111}\sigma_{\parallel}, \tag{A1}$$

$$\varepsilon_{\parallel} = \varepsilon^{111}_{\psi=90^\circ} = \left(2S_1^{111} + \tfrac{1}{2}S_2^{111}\right)\sigma_{\parallel}. \tag{A2}$$

Thus, the biaxial Poisson's ratio can be calculated from two diffraction elastic constants as

$$\nu_{\mathrm{bi}} = -\frac{\varepsilon_{\perp}}{\varepsilon_{\parallel}} = -\frac{2S_1^{111}}{2S_1^{111} + \frac{1}{2}S_2^{111}}. \tag{A3}$$

When the constants shown in Table II are employed, the calculated ratios for the (111)-textured and the normal Pd($H_{0.66}$) films are 1.01 and 1.13, respectively. The calculated ratio for the (111)-textured Pd($H_{0.66}$) film (ν_{bi} = 1.01) agrees with one reported by Ogi *et al.*[44] In the case of (111)-textured film, the equation can also be described using the single-crystal elastic compliances:

$$\nu_{\mathrm{bi}} = -\frac{2S_1^{111}}{2S_1^{111} + \frac{1}{2}S_2^{111}} = -\frac{2\left(\frac{1}{3}s_{11} + \frac{2}{3}s_{12} - \frac{1}{6}s_{44}\right)}{2\left(\frac{1}{3}s_{11} + \frac{2}{3}s_{12} - \frac{1}{6}s_{44}\right) + \frac{1}{2}s_{44}} = -\frac{4s_{11} + 8s_{12} - 2s_{44}}{4s_{11} + 8s_{12} + s_{44}}. \tag{A4}$$

Also, the proportional coefficient of Eq. (16) for (111)-textured film can be written using the single-crystal elastic compliances:

$$\frac{\nu_{\mathrm{bi}}\alpha_{\mathrm{H}}}{2S_1^{111}} = -\frac{\alpha_{\mathrm{H}}}{2S_1^{111} + \frac{1}{2}S_2^{111}} = -\frac{6\alpha_{\mathrm{H}}}{4s_{11} + 8s_{12} + s_{44}}. \tag{A5}$$

The right-hand side of the above equation is in agreement with the calculation by Wagner *et al.*[18]

[1] F. D. Manchester, A. San-Martin, and J. M. Pitre, J. Phase Equilib. **15**, 62 (1994).
[2] J. A. Eastman, L. J. Thompson, and B. J. Kestel, Phys. Rev. B **48**, 84 (1993).
[3] A. Baldi, T. C. Narayan, A. L. Koh, and J. A. Dionne, Nat. Mater. **13**, 1143 (2014).
[4] A. Ulvestad, M. J. Welland, S. S. E. Collins, R. Harder, E. Maxey, J. Wingert, A. Singer, S. Hy, P. Mulvaney, P. Zapol, and O. G. Shpyrko, Nat. Commun. **6**, 10092 (2015).
[5] G. Q. Li, H. Kobayashi, J. M. Taylor, R. Ikeda, Y. Kubota, K. Kato, M. Takata, T. Yamamoto, S. Toh, S. Matsumura, and H. Kitagawa, Nat. Mater. **13**, 802 (2014).
[6] G. Q. Li, H. Kobayashi, S. Dekura, R. Ikeda, Y. Kubota, K. Kato, M. Takata, T. Yamamoto, S. Matsumura, and H. Kitagawa, J. Am. Chem. Soc. **136**, 10222 (2014).
[7] V. Berube, G. Radtke, M. Dresselhaus, and G. Chen, Int. J. Energy Res. **31**, 637 (2007).
[8] R. Griessen, N. Strohfeldt, and H. Giessen, Nat. Mater. **15**, 311 (2016).
[9] R. Feenstra, G. J. Debruinhordijk, H. L. M. Bakker, R. Griessen, and D. G. Degroot, J. Phys. F **13**, L13 (1983).
[10] E. Lee, J. M. Lee, J. H. Koo, W. Lee, and T. Lee, Int. J. Hydrogen Energy **35**, 6984 (2010).
[11] S. Wagner, H. Uchida, V. Burlaka, M. Vlach, M. Vlcek, F. Lukac, J. Cizek, C. Baehtz, A. Bell, and A. Pundt, Scr. Mater. **64**, 978 (2011).
[12] J. Cizek, O. Melikhova, M. Vlcek, F. Lukac, M. Vlach, I. Prochazka, W. Anwand, G. Brauer, A. Mucklich, S. Wagner, H. Uchida, and A. Pundt, Int. J. Hydrogen Energy **38**, 12115 (2013).
[13] S. Wagner, T. Kramer, H. Uchida, P. Dobron, J. Cizek, and A. Pundt, Acta Mater. **114**, 116 (2016).
[14] T. P. L. Pedersen, C. Liesch, C. Salinga, T. Eleftheriadis, H. Weis, and M. Wuttig, Thin Solid Films **458**, 299 (2004).
[15] A. Pundt and R. Kirchheim, Annu. Rev. Mater. Res. **36**, 555 (2006).
[16] R. Gremaud, M. Gonzalez-Silveira, Y. Pivak, S. de Man, M. Slaman, H. Schreuders, B. Dam, and R. Griessen, Acta Mater. **57**, 1209 (2009).
[17] A. L. Roytburd, B. M. Boyerinas, and H. A. Bruck, J. Phys.: Condens. Matter **27**, 092201 (2015).
[18] S. Wagner and A. Pundt, Int. J. Hydrogen Energy **41**, 2727 (2016).
[19] P. F. Miceli, H. Zabel, J. A. Dura, and C. P. Flynn, J. Mater. Res. **6**, 964 (1991).

[20] P. M. Reimer, H. Zabel, C. P. Flynn, A. Matheny, K. Ritley, J. Steiger, S. Blasser, and A. Weidinger, Z. Phys. Chem. **181**, 367 (1993).
[21] H. Zabel and A. Weidinger, Comments Condens. Matter Phys. **17**, 239 (1995).
[22] U. Laudahn, A. Pundt, M. Bicker, U. von Hulsen, U. Geyer, T. Wagner, and R. Kirchheim, J. Alloys Compd. **293**, 490 (1999).
[23] S. J. Callori, C. Rehm, G. L. Causer, M. Kostylev, and F. Klose, Metals **6**, 125 (2016).
[24] Q. M. Yang, G. Schmitz, S. Fahler, H. U. Krebs, and R. Kirchheim, Phys. Rev. B **54**, 9131 (1996).
[25] Y. Pivak, V. Palmisano, H. Schreuders, and B. Dam, J. Mater. Chem. A **1**, 10972 (2013).
[26] T. Harumoto, T. Sannomiya, Y. Matsukawa, S. Muraishi, J. Shi, Y. Nakamura, H. Sawada, T. Tanaka, Y. Tanishiro, and K. Takayanagi, J. Appl. Phys. **113**, 084306 (2013).
[27] T. Harumoto, T. Sannomiya, S. Muraishi, J. Shi, and Y. Nakamura, J. Appl. Crystallogr. **49**, 909 (2016).
[28] U. Welzel, A. Kumar, and E. J. Mittemeijer, Appl. Phys. Lett. **95**, 111907 (2009).
[29] T. Harumoto, T. Sannomiya, S. Muraishi, J. Shi, and Y. Nakamura, J. Appl. Crystallogr. **47**, 1490 (2014).
[30] W. Voigt, *Lehrbuch der Kristallphysik* (Teubner Verlag, Berlin-Leipzig, 1928).
[31] A. Reuss, Z. Angew. Math. Mech. **9**, 49 (1929).
[32] K. Tanaka, Y. Akiniwa, T. Ito, and K. Inoue, JSME Int. J., Ser. A **42**, 224 (1999).
[33] J. D. Kamminga, T. H. de Keijser, E. J. Mittemeijer, and R. Delhez, J. Appl. Crystallogr. **33**, 1059 (2000).
[34] M. Leoni, U. Welzel, P. Lamparter, E. J. Mittemeijer, and J. D. Kamminga, Philos. Mag. A **81**, 597 (2001).
[35] V. Hauk, *Structural and Residual Stress Analysis by Nondestructive Methods* (Elsevier, Amsterdam, 1997).
[36] J. D. Eshelby, Proc. Roy. Soc. London A **241**, 376 (1957).
[37] E. Kroner, Z. Phys. **151**, 504 (1958).
[38] F. Bollenrath, V. Hauk, and E. H. Muller, Z. Metallkd. **58**, 76 (1967).
[39] R. de Wit, J. Appl. Crystallogr. **30**, 510 (1997).
[40] D. K. Hsu and R. G. Leisure, Phys. Rev. B **20**, 1339 (1979).
[41] H. Peisl, Chap. 3. Lattice Strains due to Hydrogen in Metals in *Hydrogen in Metals I*, edited by G. Alefeld and J. Völkl (Springer-Verlag, Berlin Heidelberg, 1978).
[42] ICDD cards, No. 00-046-1043.
[43] D. W. Hoffman and J. A. Thornton, J. Vac. Sci. Technol. **20**, 355 (1982).
[44] H. Ogi, M. Fujii, N. Nakamura, T. Yasui, and M. Hirao, Phys. Rev. Lett. **98**, 195503 (2007).